ELSEVIER

Journal of Fluids and Structures 26 (2010) 994–1017

JOURNAL OF FLUIDS AND STRUCTURES

www.elsevier.com/locate/jfs

Enhancement of channel wall vibration due to acoustic excitation of an internal bubbly flow

M.M. Zhang, J. Katz*, A. Prosperetti

Department of Mechanical Engineering, The Johns Hopkins University, Baltimore, MD 21218, USA

Received 11 April 2008; accepted 19 May 2010
Available online 14 August 2010

Abstract

The effect of an internal turbulent bubbly flow on vibrations of a channel wall is investigated experimentally and theoretically. Our objective is to determine the spectrum and attenuation rate of sound propagating through a bubbly liquid flow in a channel, and connect these features with the vibrations of the channel wall and associated pressure fluctuations. Vibrations of an isolated channel wall and associated wall pressure fluctuations are measured using several accelerometers and pressure transducers at various gas void fractions and characteristic bubble diameters. A waveguide-theory-based model, consisting of a solution to the three-dimensional Helmholtz equation in an infinitely long channel with the effective physical properties of a bubbly liquid is developed to predict the spectral frequencies of the wall vibrations and pressure fluctuations, the corresponding attenuation coefficients and propagation phase speeds. Results show that the presence of bubbles substantially enhances the power spectral density of the channel wall vibrations and wall pressure fluctuations in the 250–1200 Hz range by up to 27 and 26 dB, respectively, and increases their overall rms values by up to 14.1 and 12.7 times, respectively. In the same frequency range, both vibrations and spectral frequencies increase substantially with increasing void fraction and slightly with increasing bubble diameter. Several weaker spectral peaks above that range are also observed. Trends of the frequency and attenuation coefficients of spectral peaks, as well as the phase velocities are well predicted by the model. This agreement confirms that the origin of enhanced vibrations and pressure fluctuations is the excitation of streamwise propagating pressure waves, which are created by the initial acoustic energy generated during bubble formation.

Keywords: Internal bubbly flow; Channel wall vibration; Void fraction; Bubble diameter; Acoustic normal mode; Waveguide theory

1. Introduction

Bubbly-flow-induced pipe vibrations often exist in industrial heat exchangers, such as condensers, evaporators, nuclear steam generators, boilers and reboilers (Pettigrew and Taylor, 1994). Under certain conditions, these vibrations may become excessive, and may cause serious pipe failure by fatigue, fretting wear and cracking, leading to costly maintenance and loss of production. Therefore, measuring and understanding these vibrations has attracted considerable research interest in the past.

*Corresponding author.
E-mail address: katz@jhu.edu (J. Katz).

0889-9746/$ - see front matter © 2010 Elsevier Ltd. All rights reserved.
doi:10.1016/j.jfluidstructs.2010.06.003

Previous studies of this problem may be divided into two groups: one dealing with flows with vapor bubbles and another with flows with gas bubbles. The studies in the first group are more numerous as the situation here is closer to that of many practical applications. Representative studies are those by Pettigrew and Gorman (1981), Feenstra et al. (1995), Mann and Mayinger (1995) and Nakamura et al. (2002) who introduced tube bundles into steam bubbly cross-flows to approximate the situation encountered in heat exchangers. These experiments are expensive and difficult and require complex experimental facilities. For these reasons, and also in view of their inherent interest, other researchers have studied similar arrangements in which the bubbles consist of an incondensable gas rather than vapor (see, e.g., Gorman, 1971; Joo and Dhir, 1994; Iijima et al., 1995; Uchiyama, 2003; Heilker and Vincent, 1981; Pettigrew et al., 1985, 2001, 2005). The two situations are physically different, although they exhibit some similarities, such as the excitation of pipe vibrations, as shown by Weaver and Fitzpatrick (1988) and Pettigrew et al. (2002). All these investigations, with both vapor and gas bubbles, show that bubbly flows cause a substantial increase in the amplitude of pipe vibrations. Two main mechanisms, as summarized by Weaver et al. (2000), are responsible for the enhanced vibrations. The first is fluidelastic instability, which occurs beyond a critical flow rate, when interactions among individual tubes generate excitation forces on the surrounding tubes. These forces, which vary with the void fraction, reduced velocity and flow pattern, are both proportional to tube displacements and in-phase with tube velocities, leading to great enhancement in the vibration amplitudes. The second mechanism is random turbulence excitation. The resultant excitation force by the presence of bubbles, dependent on flow conditions and void fraction, increases broadband pressure fluctuations near the tubes and consequently tube vibrations.

It is worth mentioning that the previous studies only focused on the channel vibrations caused by external bubbly flow. To the best of our knowledge, channel vibrations induced by internal bubbly flow have never been investigated before. However, according to the Heat Transfer and Fluid Flow Service of Canada (HTFS; Pettigrew and Taylor, 1994), more than half of the process heat exchangers operate in an environment of two-phase bubbly flow, which inherently involves also internal bubbly flows. Thus, it is of engineering significance to investigate the role and contribution of internal bubbly flow on the vibrations as, our group has done in recent years. In a first stage of this research program, the gas bubble case is studied by introducing CO_2 gas bubbles into a channel flow, and examining the channel vibrations. Following two conference papers with preliminary results (Pelletier et al., 2006; Zhang and Katz, 2007), this paper provides both data and analysis of the observed substantial increase in channel wall vibrations and wall pressure fluctuations after introducing bubbles into the flow. We first show that vibration and pressure fluctuation spectra vary with void fraction, characteristic bubble size, and location within the channel. Subsequent analysis then focuses on the observed spectral peaks and their variations along the channel. We show that a mathematical model of sound propagation and attenuation in a bubby medium using waveguide theory, based on earlier work of Commander and Prosperetti (1989) and Lu (1990), predicts and elucidates the observed trends. We start with a description of the test facility and data acquisition procedure in the following section.

2. Experimental set-up and procedures

The experiments have been performed in a closed-loop water channel facility, which was used in previous studies of flow-induced vibrations (Gopalan et al., 2004), and then substantially modified for generating flows with controlled bubble sizes and spatial distributions for the present work. Fig. 1(a) shows a schematic of the facility. The water is driven by two 11 kW centrifugal pumps, located in the basement below the facility to prevent any pump cavitation issues, and connected to the facility by flexible hoses. Three strategies are implemented to isolate the test channel from external excitations. First, the settling chamber is mounted on vibration-isolated supports, and the test channel is supported by vibration-isolated padding. Second, long flexible hoses with varying lengths are used for connecting components of the test loop to reduce the effect of pump-induced vibrations or other facility resonances on the channel flow. Third, water is introduced into the settling chamber (see, Fig. 1(a)), through perforated plates covering three of the chamber's walls, while the remaining wall has a port through which the bubble injector is inserted. By doing so, the primary extraneous unsteady loading, namely the signatures of non-uniformities generated by upstream pipe flows and pumps are greatly reduced. The channel is also supported by a heavy structure that does not vibrate at any meaningful level when there is flow, with or without bubbles, in the facility. The bubbles are introduced in the settling chamber, and the bubbly water passes through a honeycomb and a streamlined nozzle before entering a 0.15 m × 0.15 m cross-section, 2 m long channel. Suction of the boundary layer on the channel wall, followed by tripping using a series of grooves, reduces the effects of upstream disturbances, and generates a classical, fully turbulent boundary layer profile (Gopalan et al., 2004). The test channel is aligned vertically to prevent gravity-induced streamwise variations in bubble distribution. It is essential to remove and reintroduce bubbles continuously so that their size and spatial distribution can

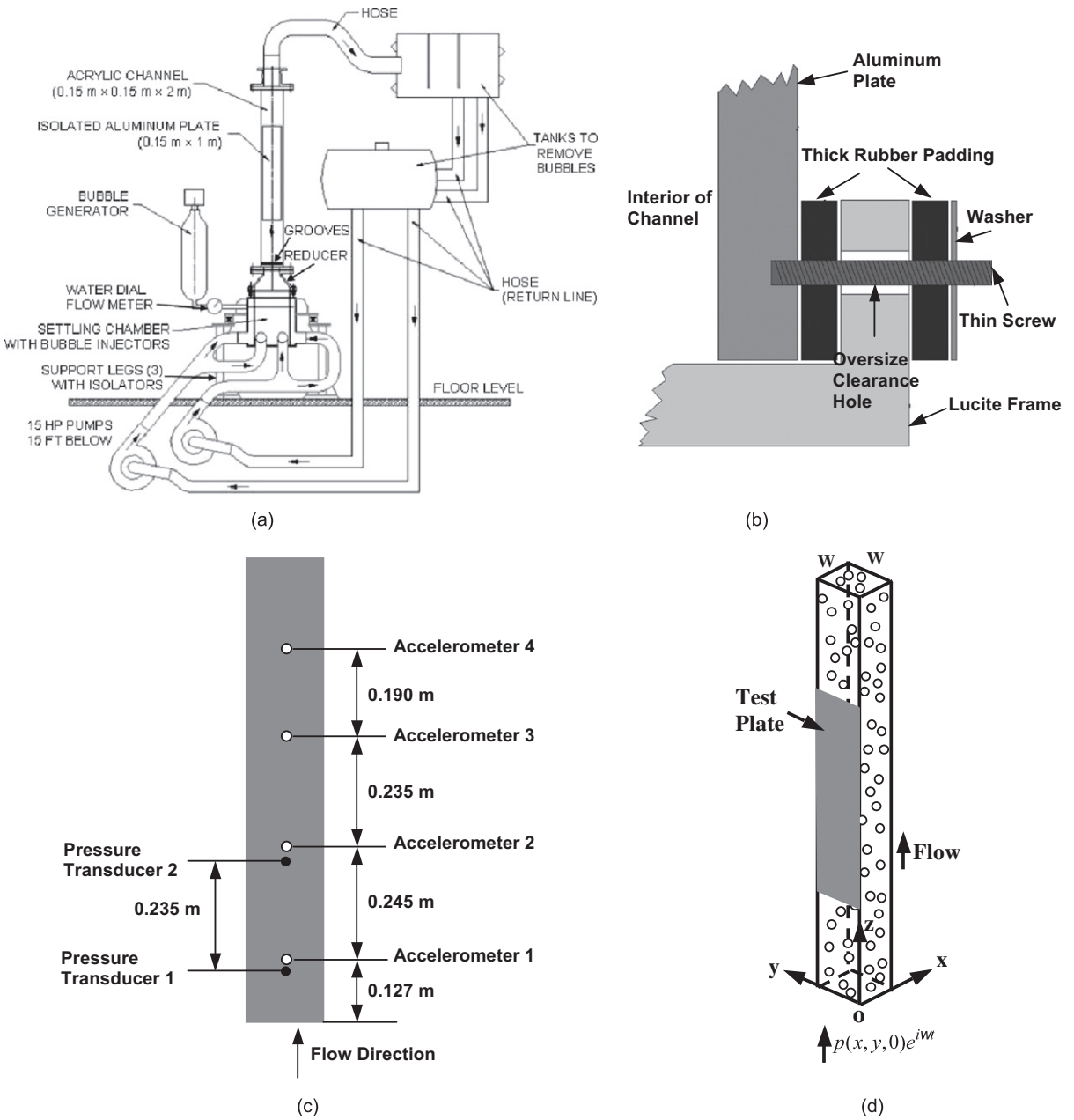

Fig. 1. Experimental set-up: (a) The quiet bubbly flow test facility; (b) schematic of vibration isolated plate mounting; (c) the test plate and location of accelerometers and pressure transducers and (d) schematic of infinitely long rigid channel model.

be controlled. Thus, after leaving the test channel, the bubbly water flows into two large tanks (~4000 l total) whose purpose is to remove the bubbles by buoyancy prior to returning the water to the pumps. A curved water path within these tanks helps in separating the bubbles, and provides ample time for the bubbles to rise to the free surface of the upper tank, which is open to the atmosphere. Thus, flow conditions upstream of the channel are the same with or without bubble injection.

To measure the channel wall vibration, an aluminum flat plate, with a length of 1 m, a width of 0.15 m and a thickness of 6.25 mm, is embedded in one of the test channel walls, flush with the internal surface. As illustrated in Fig. 1(b), the plate is mounted between thick rubber gaskets, which isolate it and prevent any direct contact with other rigid components. The mounting screws pass through oversize holes in the Lucite frame of the channel, and the only

contact that the plate has with the frame is through the thick rubber gaskets, isolating it from frame vibrations. Consequently, the bubbly flow provides most of the plate excitation. Comments on how well the present isolation system works are provided in Pelletier et al. (2006). When we hit the hoses or settling camber, traces of several damped spectral peaks appear in the signals of the accelerometers mounted on the test plate. However, all of these peaks appear well below 200 Hz, while the enhanced vibrations shown in the next section and the analysis that follows occur at higher frequencies. Below 200 Hz, introduction of bubbles has little impact on the vibrations. The vibrations are measured using four low-noise Kistler accelerometers (Model 8784A5) with a sensitivity of 1.035 V/g. These accelerometers are attached along the midline of the plate in the streamwise direction using a cyano-acrylate adhesive, as shown in Fig. 1(c). They are located 0.127, 0.372, 0.607 and 0.797 m from the plate leading edge and are referred to in this paper as accelerometers 1, 2, 3 and 4, respectively. In addition, wall pressure fluctuations are measured at two locations using two flush-mounted, 2.5 mm diameter, Endevco miniature piezoresistive pressure transducers (Model 8510B-1) that have a sensitivity of 2.9×10^{-5} V/Pa. These sensors are installed near accelerometers 1 and 2, and referred to as transducer nos. 1 and 2, respectively (see Fig. 1(c)). To conveniently describe the location in the channel, a coordinate system is used with x, y in the horizontal plane and z in the streamwise direction, and the origin placed at one corner of the channel (Fig. 1(d)).

The flow is seeded with bubbles by injecting a supersaturated solution of carbon dioxide (CO_2) and water into the settling chamber. A similar technique was used by Martínez-Bazán et al. (1999). As illustrated in Fig. 2, to obtain saturated water at high pressure, the water is sprayed into a CO_2 filled chamber, which is kept at a pressure of 1.7 MPa. The resulting saturated solution is injected through an array of stainless steel porous tubes located in the settling chamber. Each tube is 0.35 m long, and has an inner diameter of 3.2 mm, an outer diameter of 9.6 mm and a pore size of 0.2 μm. Due to the pressure drop across the porous wall of the tubes, the dissolved CO_2 becomes supersaturated, causing nucleation of bubbles, which are entrained by the water. Subsequent mixing with the main water flow along with introduction of surfactants in some cases (see below) greatly reduces the likelihood of coalescence of the bubbles.

The main characteristics of the CO_2 bubble cloud, i.e., bubble diameter (d) and volumetric void fraction (v), are controlled and measured, as described below. The present measurements and analysis are restricted to steady flow conditions and low void fractions, less than 2.34%, and bubbles in the 0.37–1.2 mm range, although we have performed preliminary measurements at higher concentrations and with larger bubbles (Pelletier et al., 2006). The bubble diameter

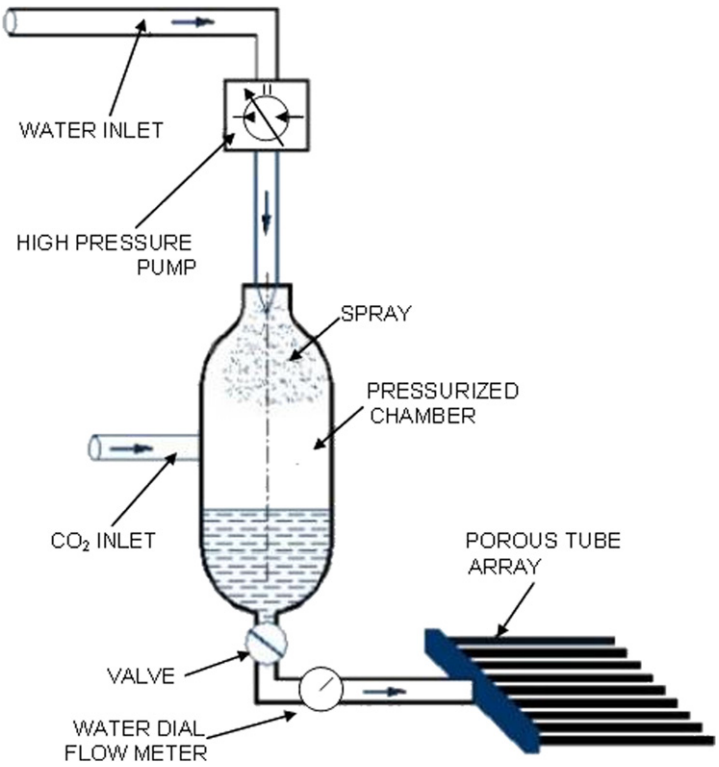

Fig. 2. The bubble generator and injector.

is regulated by adding a surfactant (Pentanol-3) to the flow, at concentrations of 0, 6 and 12 ppm. The surfactant reduces bubble surface tension and inhibits coalescence with a minimal effect on liquid viscosity (Shen et al., 2006). The corresponding most abundant bubble diameters are 1.20, 0.69 and 0.37 mm, as illustrated by the typical magnified images in Fig. 3. At low concentration, varying the injection rate of supersaturated liquid has little effect on the characteristic bubble size. The bubble sizes are measured by illuminating a small sample area, 10 mm × 10 mm, of the flow field with a 6.0 mm thick, 120 mJ/pulse, Nd:YAG laser sheet. The illuminated central plane is aligned with the streamwise direction and perpendicular to the test plate. The flow is seeded with fluorescent dye (Rhodamine-WT), which essentially converts the entire illuminated plane to a light source. Bubbles passing through this plane becomes clearly visible, permitting accurate measurements of their sizes. Since the wavelength of the green laser light is smaller than that of yellow fluorescent light, a high-pass optical filter is positioned in front of a camera to block the laser light, but allowing the light reflected from bubbles to pass. Images are recorded using a 2 k × 2 k pixels CCD camera, which is synchronized with the laser.

Bubble sizes are measured automatically using blob analysis software developed specifically for this purpose, which provides the size distribution of bubbles in each image. The bubble size distribution measurements have been conducted at two sections, near accelerometers 1 and 4, along lateral directions. Fig. 4 compares the typical bubble size distributions. For each section, the bubble images are recorded at three lateral locations, corresponding to 38 mm from test plate, middle of the channel and 38 mm from the channel wall opposite to the plate. We have not seen any statistically significant differences in bubble size distributions across the channel, and consequently only show in Fig. 4 sample histograms of size distributions for the section located closest to the channel wall near accelerometers 1 and 4. As is evident, in all cases, there is a dominant bubble size, which we use this to define the characteristic diameter. Although the fraction of bubbles with that specific size decreases slightly along the channel, presumably due to coalescence, the same diameter still dominates over the entire channel. The same conclusion applies to all bubble sizes and void fractions, including those not shown here. These results suggest that the spatial distribution of bubbles in the test channel is very nearly uniform, and we will assume so for the analysis that follows.

To estimate v, we assume that all bubbles move uniformly in the test channel and the time for bubbles filling the square channel with length L and width W can be expressed as $t = L/(U_w + U_{slip})$, where U_w is the mean flow velocity of water and U_{slip} the buoyancy-induced slip velocity between bubbles and water. Then, the volume of CO_2 bubbles in the channel is $Q_{CO_2}L/(U_w + U_{slip})$, where Q_{CO_2} is the volumetric flow rate of CO_2. Thus, the void fraction is

$$v = \frac{Q_{CO_2}}{U_w W^2 + U_{slip} W^2}. \tag{1}$$

The mean flow velocity of water U_w is measured using an ultrasonic Doppler flow meter, Dynasonics 901 (uncertainty ~2%), attached to the pipe downstream of the facility. To estimate U_{slip}, we assume that the buoyancy of an individual bubble is balanced by the drag force, giving $U_{slip} = \sqrt{4dg/3C_D}$. Here, C_D is the drag coefficient, calculated using $C_D = 24(1 + 0.15\mathrm{Re}^{0.687})/\mathrm{Re}$ (Schiller and Nauman, 1933; Sridhar and Katz, 1995), where $\mathrm{Re} = U_{slip}d/n$. The value of Q_{CO_2} can be estimated from a mass balance of CO_2 injected into the facility (Merkle and Deutsch, 1992), taking advantage of the fact that the water prior to injection of CO_2 is saturated. Using ideal gas laws as well as solubility of

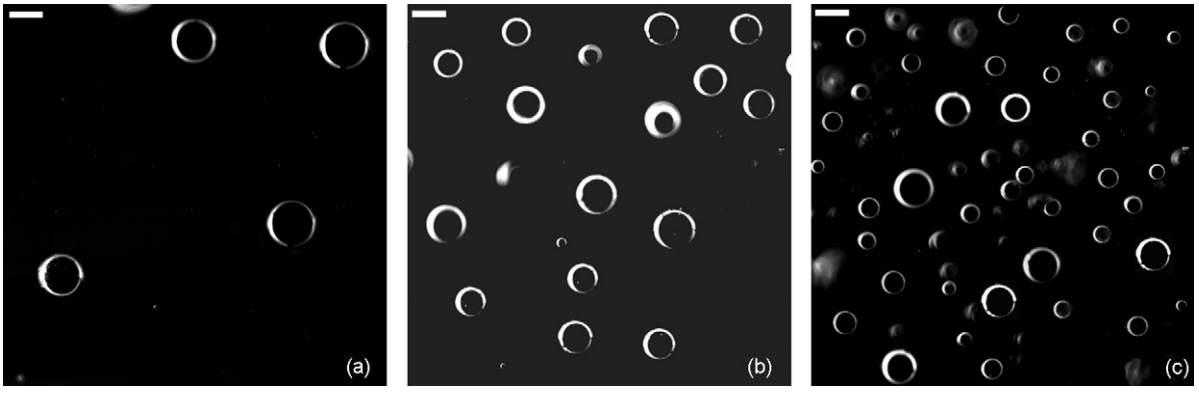

Fig. 3. Typical images of bubble clouds for varying characteristic bubble diameters (d): (a) $d = 1.20$ mm; (b) $d = 0.69$ mm and (c) mostly $d = 0.37$ mm. White scales are 1 mm.

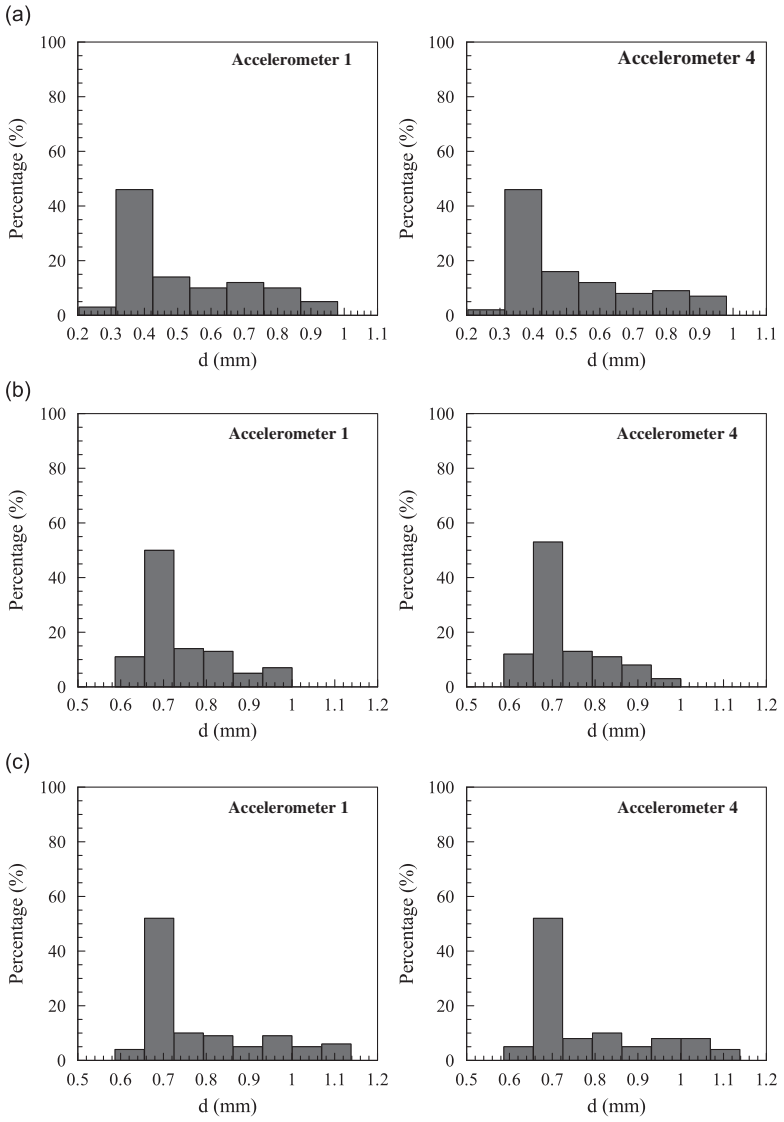

Fig. 4. Typical bubble size distributions measured at two 10×10 mm^2 sections of the central plane of the channel, which are closest to the channel wall near accelerometers 1 and 4. Measurements are conducted for different bubble diameter d and void fraction v: (a) $d = 0.37$ mm, $v = 1.15\%$; (b) $d = 0.69$ mm, $v = 1.15\%$ and (c) $d = 0.69$ mm, $v = 2.29\%$.

CO_2 as a function of pressure and temperature, and assuming thermodynamic equilibrium,

$$Q_{CO_2} = 1000 Q^{inj} \rho_w C^{20^o}_{1.7\,MPa} RT/\overline{P}[(1 - C^{20^\circ}_{1.7\,MPa}) M_{H_2O} + C^{20^\circ}_{1.7\,MPa} M_{CO_2}], \quad (2)$$

where Q^{inj} stands for the injection rate of saturated water at 1.7 MPa through the porous tubes, ρ_w is the density of water, $C^{20^\circ}_{1.7\ MPa} = 0.012$ (Carroll et al., 1991) the mole fraction of saturated CO_2 at 1.7 MPa and 20 °C, R is the universal gas constant (= 8.31 m^3 Pa K^{-1} mol^{-1}), T is the absolute temperature, M is the molecular weight and $\overline{P}$ is the mean pressure in the channel at the exit from the porous tubes ($\overline{P} = \overline{P}_a + \rho_w gh$, $\overline{P}_a$ is the atmospheric pressure and h is the distance from porous tubes to the free water surface). In this paper, three low void fraction cases, i.e., $v = 0.64\%$, 1.15% and 2.29%, are investigated.

One can also estimate the gas volume fraction by counting the bubbles passing through the 6 mm thick light sheet. We have compared results obtained in this way with those obtained using mass balance. The results fall within 20% of the estimation based on mass balance, providing reasonable support for using the former in this paper.

3. Effect of internal bubbly flow on plate vibration

Experiments were first conducted to investigate the effect of flow velocity on the plate acceleration in order to obtain a baseline database without bubbles. Each data set was recorded at 70 kHz for 15 s. For analysis, data were divided into segments and the frequency content of each one was calculated using Matlab-based fast Fourier transform (FFT) after removing mean values and detrending (see e.g. Emery and Thomson, 1997). The resulting spectra were averaged. Examples of such averaged power spectral densities at two typical velocities of 1 and 2 m/s are presented in Fig. 5(a). The vibrations at 2 m/s are at most 25 dB higher than the no-flow case (i.e., the noise level of the sensor), while those at 1 m/s are only 15 dB higher than the base level. In the present paper, mostly for convenience, we focus on the effect of bubbles at 1 m/s flow velocity, i.e., Reynolds number based on channel width and pure water viscosity of 1.45×10^5. Earlier data at higher velocity are similar and can be found in Pelletier et al. (2006). There are two prominent peaks, one around 700 Hz and the other around 2820 Hz. The normal modes of a simply supported plate are given by (see e.g. Genta, 1999)

$$f_n^{(n_1,n_2)} = \frac{\pi}{2}\left[\left(\frac{n_1}{L_{\mathrm{al}}}\right)^2 + \left(\frac{n_2}{W_{\mathrm{al}}}\right)^2\right]\sqrt{\frac{E_{\mathrm{al}}H_{\mathrm{al}}^2}{12\rho_{\mathrm{al}}(1-\upsilon_{\mathrm{al}}^2)}}, \quad n_1, n_2 = 0, 1, 2\ldots, \tag{3}$$

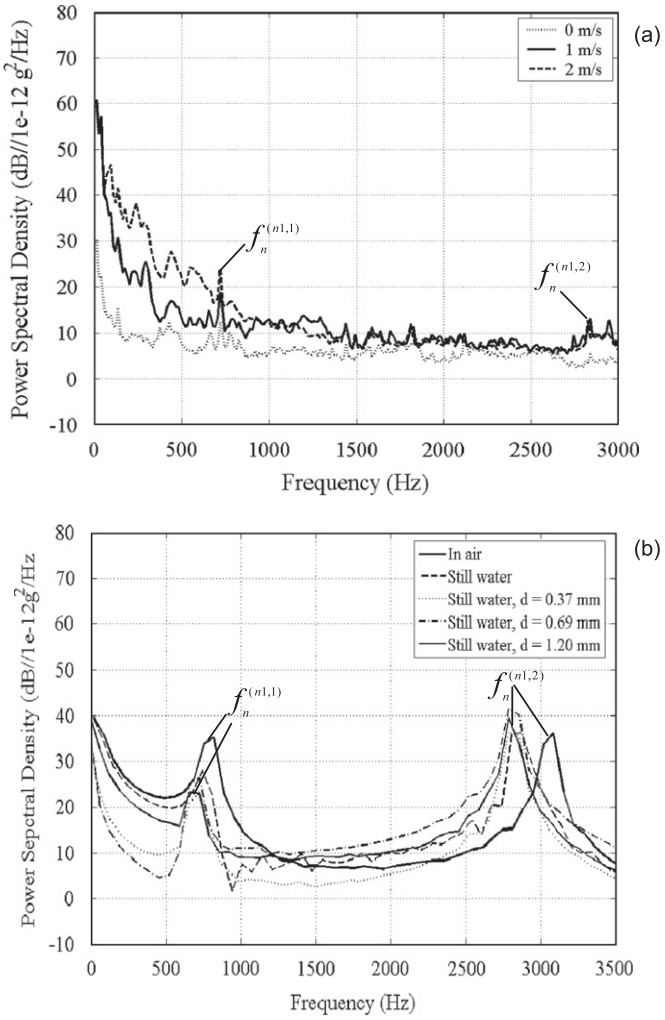

Fig. 5. Power spectral density of plate acceleration, as measured by accelerometer 3: (a) effect of flow velocity with no bubble injection; (b) impulse frequency response of the plate for air and for still water with and without bubbles. The bubble void fraction v is 0.64%. $n_1 = 0$ or 1.

where L_{al} and W_{al} are the length and width, H_{al} the thickness, E_{al} Young's modulus, ρ_{al} density and υ_{al} the Poisson ratio of aluminum. Values of n_1 and n_2 refer to the order of the longitudinal and spanwise modes of the plate, respectively. Some results calculated from this relation are presented in Table 1. This equation is not directly applicable to our situation because it ignores the loading of the water on the plate. To investigate the effects due to this aspect of the problem, we measured the plate impulse response by hitting it while the facility contained air, still water and still water with bubbles of various sizes and the same $v = 0.64\%$. These results are shown in Fig. 5(b), where it is seen that the peaks in air occur at a higher frequency than in water, as expected. From the results of Table 1, the measured peaks in air are close to the modes (0,1), (1,1) and (0,2), (1,2). Although we do not use here an analogous formula for bubbly water, it appears more than likely that the peaks measured with pure or bubbly water correspond to the same modes. It should be noted that these results, with standing water, are very close to the analogous ones with flowing water shown in Fig. 5(a). The vibrations of the same plate mounted in a somewhat different set-up (the same channel, but without bubbles), were measured by Gopalan et al. (2002) who characterized the vibrations as well damped. Based on the results in Fig. 5b, the damping coefficient is about 0.1 at 500 Hz.

After these preliminary measurements, we systematically investigated effects of void fraction v and characteristic bubble diameter d on the plate vibrations. Fig. 6 displays typical spectra of accelerometer 1 for the same d (0.69 mm), demonstrating the effect of v on the plate acceleration. Obviously, even at as low a void fraction as $v = 2.29\%$, the plate vibrations are strongly enhanced by up to 27 dB, compared to the flow without bubbles, over a broad frequency range, but especially above 250 Hz. The corresponding overall rms value of the plate acceleration, presented in Table 2,

Table 1
Plate mode frequencies ($f_n^{(n_1,n_2)}$) estimated using Eq. (3), and bubble natural frequencies (f_0^d) estimated using Eq. (4).

$f_n^{(0,n_2)}$	$f_n^{(0,1)}$	$f_n^{(0,2)}$	$f_n^{(0,3)}$	$f_n^{(0,4)}$	$f_n^{(0,5)}$
(kHz)	0.67	2.7	6.1	10.8	16.9
$f_n^{(1,n_2)}$	$f_n^{(1,1)}$	$f_n^{(1,2)}$	$f_n^{(1,3)}$	$f_n^{(1,4)}$	$f_n^{(1,5)}$
(kHz)	0.69	2.8	6.4	11.0	17.7
f_0^d	$f_0^{1.2}$	$f_0^{0.69}$	$f_0^{0.37}$		
(kHz)	4.6	8.0	15.6		

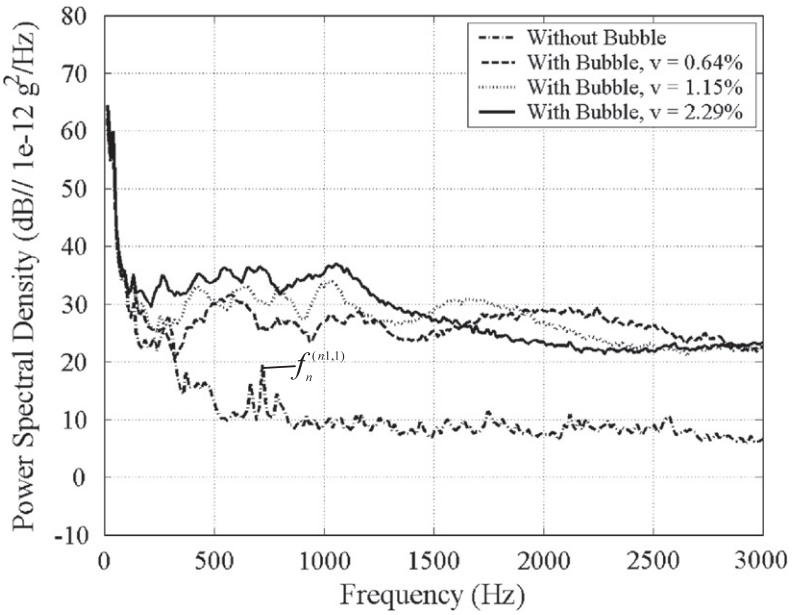

Fig. 6. Sample power spectral densities of plate acceleration, as measured by accelerometer 1, for the same characteristic bubble diameter ($d = 0.69$ mm) but different void fractions (v). $n_1 = 0$ or 1.

Table 2
Typical overall rms values of the plate accelerations for different void fractions v but the same bubble diameter d=0.69 mm and for different d but the same v=0.64%.

d = 0.69 mm	No bubbles	v = 0.64%	v = 1.15%	v = 2.29%
rms (m/s^2)	0.0035	0.0236	0.0337	0.0529
v = 0.64%	No bubbles	d = 0.37 mm	d = 0.69 mm	d = 1.20 mm
rms (m/s^2)	0.0035	0.0223	0.0236	0.0307

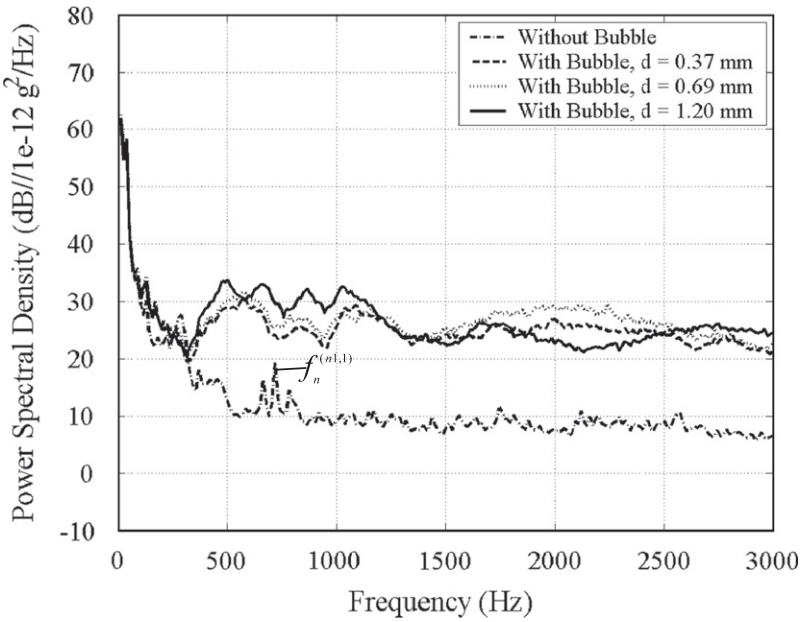

Fig. 7. Sample power spectral densities of plate acceleration, as measured by accelerometer 1, for the same void fraction (v = 0.64%) but different characteristic bubble diameters. n_1 = 0 or 1.

reaches 15.1 times that without bubbles. The peak near the mode frequency of the plate ($f_n^{(n_1,1)}$, n_1 = 0 or 1) becomes invisible in the spectra of bubbly flows, suggesting that the enhancement of the vibrations is not associated with these modes. Note that several peaks appear within the 250–1200 Hz frequency range. As we show later, the frequencies of these peaks match the acoustic mode frequencies of the bubbly channel. In addition, two phenomena can be readily noted. First, increasing v significantly increases the intensity of vibrations. Second, with increasing v, the left-most spectral peak (e.g. at ~250 Hz for v = 2.29%) moves to a lower frequency.

The plate response in the low frequency range, i.e., less than 200 Hz, is little dependent on the bubbles. We have devoted a considerable effort to this frequency range by repeatedly measuring the vibrations and we can assert with confidence that the introduction of bubbles has little impact on this spectral range. On the basis of impulsive excitation of different parts of the facility, we believe that these low-frequency vibrations are dominated by the vibrations of the flexible hoses in the facility. The effect of bubbles is mostly manifested in the 250–1200 Hz range and, to a lesser extent, higher frequencies.

Fig. 7 presents typical examples demonstrating the effect of bubble diameter d on the acceleration spectra for v = 0.64%, as measured by accelerometer 1. Compared with the no-bubble case, the acceleration of the plate vibration above 250 Hz increases by up to 20 dB, and the overall maximum rms value, measured for d = 1.20 mm, is augmented 8.8 times. Although the plate vibration increases with increasing d, as the rms values indicate, this trend does not persist over the entire frequency range. Furthermore, the spectral peaks do not seem to shift significantly with varying d. Evidently, the effect of d is much less than that of v. In evaluating the implication of this trend, note that the natural

frequency (f_0^d) of the largest bubble in the present study exceeds 4.6 kHz, i.e., higher than the frequency range presented in Figs. 6 and 7, where the effect of introducing bubbles on plate vibrations is most prominent. The analysis in the following sections of this paper focuses on explaining and modeling phenomena occurring in this range.

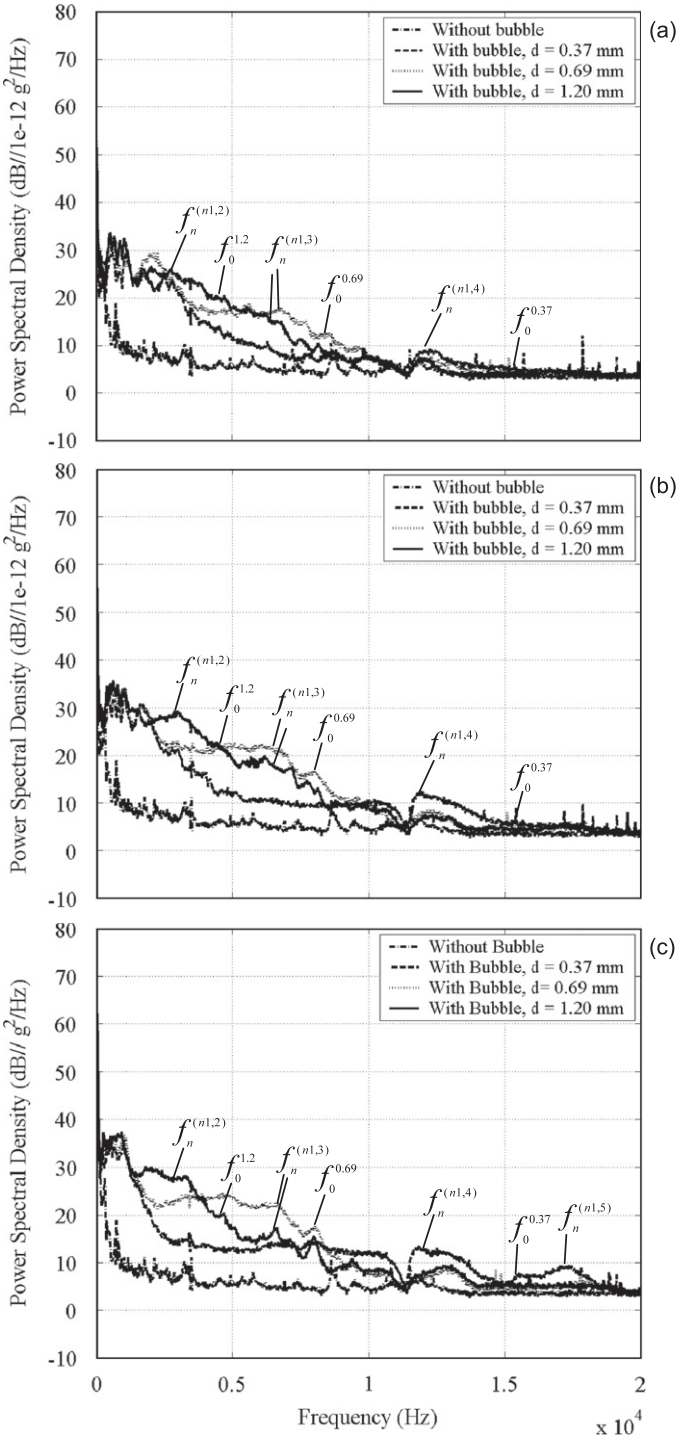

Fig. 8. Effect of bubble characteristic diameter d on the power spectral density of plate acceleration, as measured by accelerometer 1, with spectra extending to high frequency range: (a) $v = 0.64\%$; (b) $v = 1.15\%$; and (c) $v = 2.29\%$. $n_1 = 0$ or 1.

However, it would be instructive to examine briefly a wider frequency range that includes natural frequencies, f_0^d, of individual bubbles, where the superscripts indicate bubble diameter. Neglecting effect of surface tension, the natural frequency f_0 can be estimated using (Plesset and Prosperetti, 1977)

$$f_0^d = \frac{1}{\pi d}\left(\frac{3\kappa\overline{P_a}}{\rho_w}\right)^{1/2}, \tag{4}$$

where κ is the polytropic index (= 1 for the presently assumed isothermal case). Values of f_0^d for the present study are also presented in Table 1. Extending the range of the spectra from 3 to 20 kHz, Fig. 8 shows typical accelerometer 1 results for different v and d. Several additional broad peaks emerge in the extended frequency range, but they are much weaker than those appearing in the 250–1200 Hz range. For the same d, the magnitudes of the high frequency peaks increases with void fraction. In these figures, the natural frequencies of individual bubbles, 4.6, 8.0 and 15.6 kHz (Eq. 4) for $d = 1.20$, 0.69 and 0.37 mm, respectively, are labeled as $f_0^{1.2}$, $f_0^{0.69}$ and $f_0^{0.37}$. In some cases, there are distinct spectral peaks close to the bubble natural frequency, e.g. $f_0^{0.69}$, and in other cases, they are less obvious, e.g. $f_0^{1.2}$ at the low void fractions. The plate mode frequencies, labeled as $f_n^{(n_1,2)}$, $f_n^{(n_1,3)}$, $f_n^{(n_1,4)}$and $f_n^{(n_1,5)}$, with $n_1 = 0$ or 1, as estimated using Eq. (3) and summarized in Table 1, are also indicated. In some cases, but not in all of them, there is a spectral peak close to the mode frequency. There are also spectral peaks that do not match either group.

The results in Fig. 8 and Table 1 show that there is little match between the natural frequencies of individual bubbles and the plate modes, most of which are at a significantly lower frequency. However, the fact that vibrations at (some of the) plate mode frequencies are associated with the presence of bubbles indicates that there is a mechanism capable of transferring excitation energy to the plate. One possibility involves enhancement of turbulence by the bubbles, which in turn excites the plate, as discussed in the next section. However, there is another mechanism capable of transferring the bubble acoustic energy from high to low frequencies. A similar situation is encountered when oceanic ambient noise is produced by breaking waves at a much lower frequency than that of individual bubbles (Oğuz, 1994; Tkalich and Chan, 2002). The current understanding of this phenomenon relies on the damping of the single-bubble oscillations, which broadens the bubble frequency peaks, and confers to their acoustic emission a significant width capable of overlapping with neighboring plate modes. In view of the much lower sound speed in a bubbly liquid, the radiation damping of bubble oscillations may be expected to increase (see Eq. (11) and discussion below). Furthermore, since bubbly liquids are strong acoustic absorbers, the width of the plate modes may also be significantly broadened. Clearly, our present attempt to correlate the co-occurrence of bubble and plate resonances as a result of broadening of spectral peaks is speculative at this point and requires considerable more analysis and testing. Considering the complexity involved, and the smaller magnitude of these peaks, we defer such an analysis to future work. Our modeling effort focuses on the very large peaks in the 250–1200 Hz range.

4. Streamwise evolution of plate vibration and associated wall pressure fluctuation

Representative vibrations and pressure fluctuations spectra for each accelerometer and pressure transducer are presented in Figs. 9–12; Figs. 9 and 10 showing data for $v = 0.64\%$ and 2.29% while keeping $d = 1.20$ mm, and Figs. 11 and 12 comparing data for $d = 0.37$ and 1.20 mm, while keeping $v = 1.15\%$. Starting with the sensors located closest to the origin of the bubbles, several distinct peaks are evident in the spectra presented in Figs. 9(a)–12(a). They are marked and referred to as $f_{d,v}^{mn}$. Here, the subscripts refer to bubble diameter and void fraction, and the superscripts m and n represent different acoustic bubbly channel modes, m in a direction perpendicular to the plate (x direction), and n parallel to it (y direction). These designations are used for comparisons with model predictions, as described in the next section. As is evident from comparing Figs. 9(a)–10(a), and Figs. 11(a)–12(a), for the same d and v, the frequency of spectral peaks of acceleration and pressure are very similar.

However, the strong/distinct peaks of accelerometer 1 and transducer 1 decay in the streamwise direction at rates that seem to vary with void fraction, characteristic bubble diameter and mode frequency. The peaks in spectra of accelerometers 2–4 and transducer 2 are clearly smaller. Keeping the same diameter and same mode, the acceleration spectral peaks decay faster with decreasing void fraction, e.g. those at $v = 0.64\%$ compared to those at $v = 2.29\%$ (Fig. 9). For example, the $f_{1.2,0.64\%}^{11}$peak decreases by 22.8% from accelerometer 1 to accelerometer 4, while $f_{1.2,2.29\%}^{11}$ only decreases by 2.5% (Figs. 9(a) and (d)). Second, for the same void fraction and same mode, the peaks decay faster with decreasing bubble diameter, e.g. for $d = 0.37$ mm bubbles compared that $d = 1.20$ mm case (Fig. 11). For example, the magnitude at $f_{0.37,1.15\%}^{11}$ decreases by 22.6% from accelerometer 1 to accelerometer 4, while $f_{1.2,1.15\%}^{11}$ decreases by 12.5% (Figs. 11(a) and (d)). Third, for the same v and d, the peak diminishes more quickly with increasing frequency, a trend

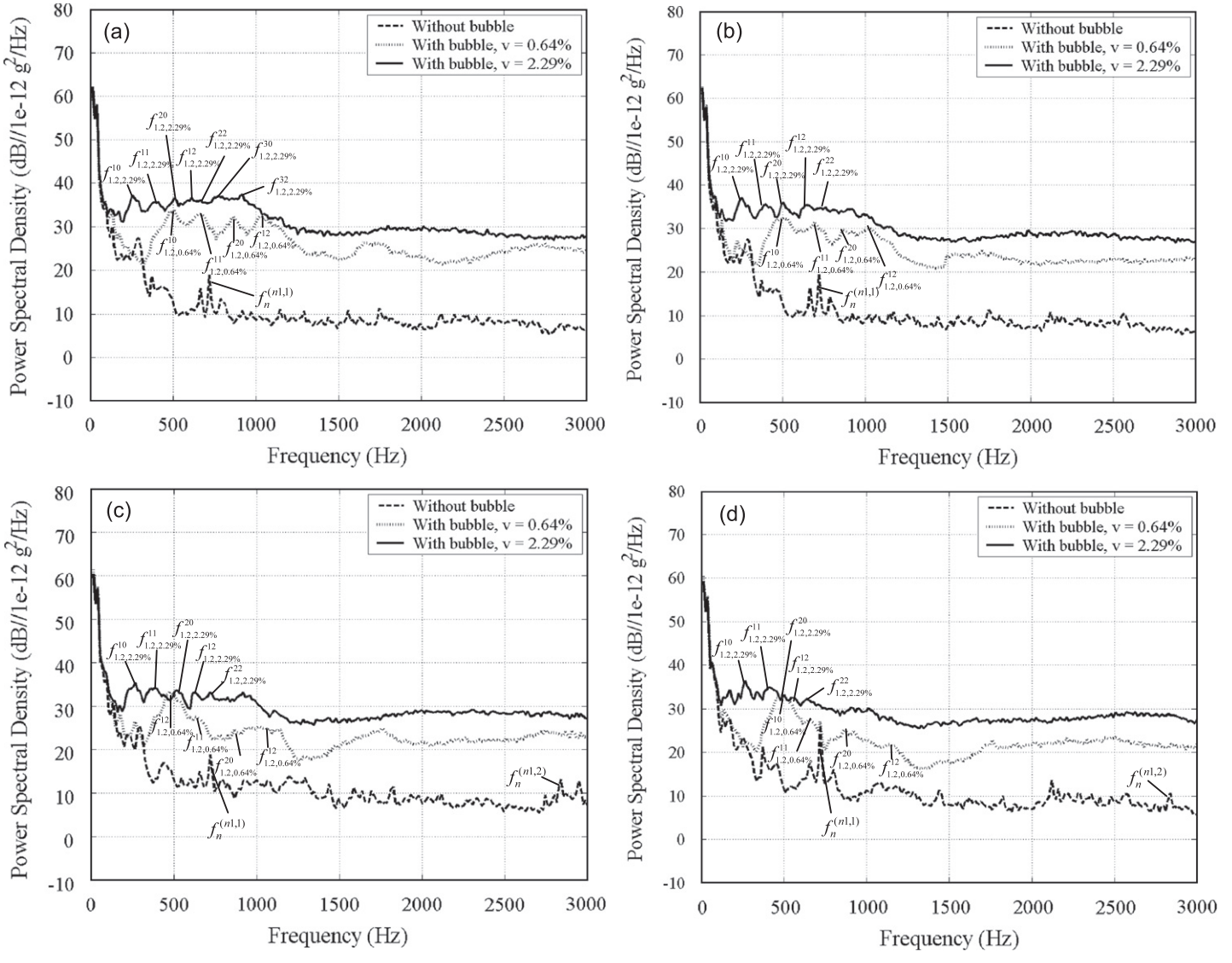

Fig. 9. Power spectral densities of plate acceleration for $d = 1.20$ mm but different void fractions, as measured by accelerometers: (a) no. 1; (b) no. 2; (c) no. 3; (d) no. 4. $n_1 = 0$ or 1.

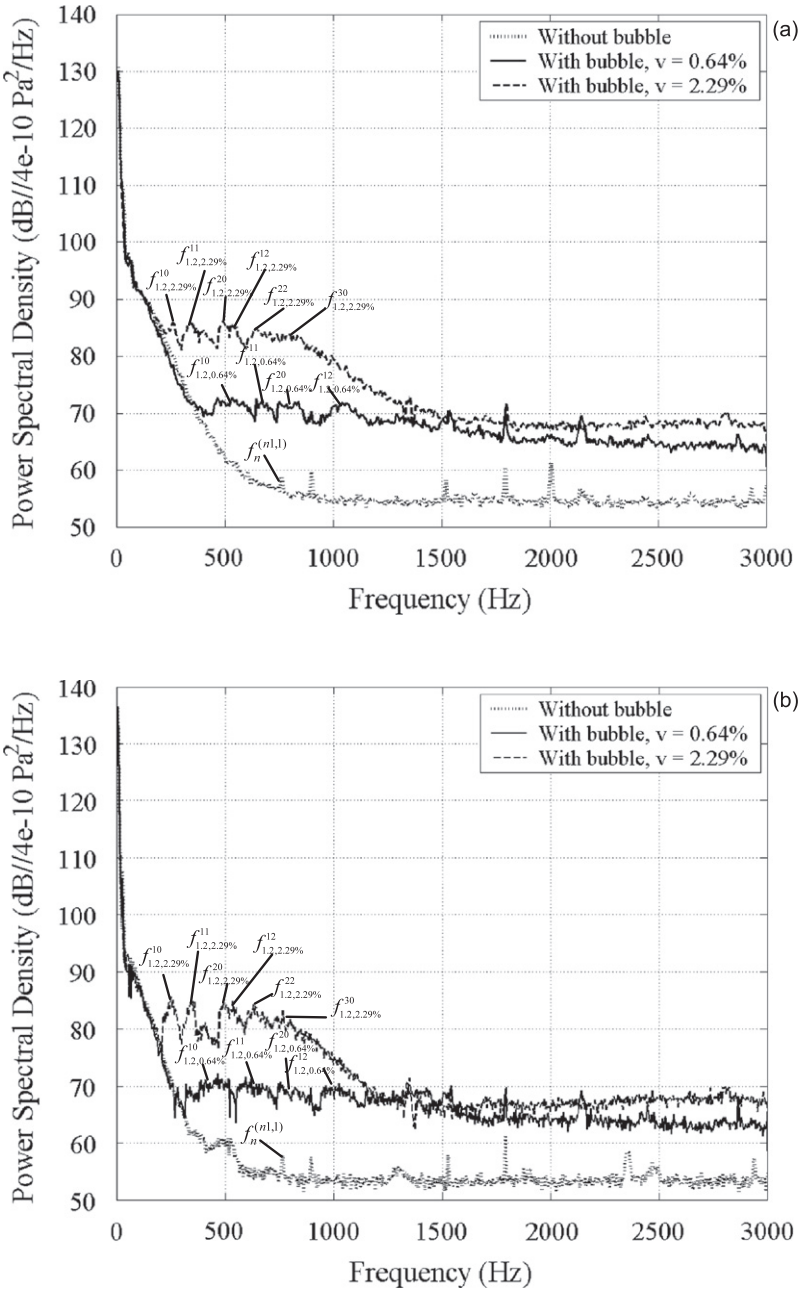

Fig. 10. Power spectral densities of wall-pressure fluctuations for $d=1.20$ mm, but at different void fractions, as measured by pressure transducer: (a) no. 1; (b) no. 2. $n_1 = 0$ or 1.

that is particularly obvious by comparing accelerometer 1 spectra to those at other locations (Figs. 9 and 11). Very similar decay trends can also be observed by comparing the spectra of the two pressure transducers (Figs. 10 and 12).

In observing the formation of spectral peaks, one wonders what is the energy source for the substantial increase in plate vibrations, and their trends with void fraction. A first possibility is an increase in turbulence level in the bubbly flow, as reported in several studies, e.g. Lance and Bataille (1991) and Shawkat et al. (2007). Although it is reasonable to expect that the elevated turbulence would contribute to increased vibrations, the observed decay of spectral peaks along the channel is inconsistent with a primary role for this mechanism. Since the spatial distribution of bubbles does not change significantly along the channel, their effect on the local turbulence should also not change appreciably. Yet, the

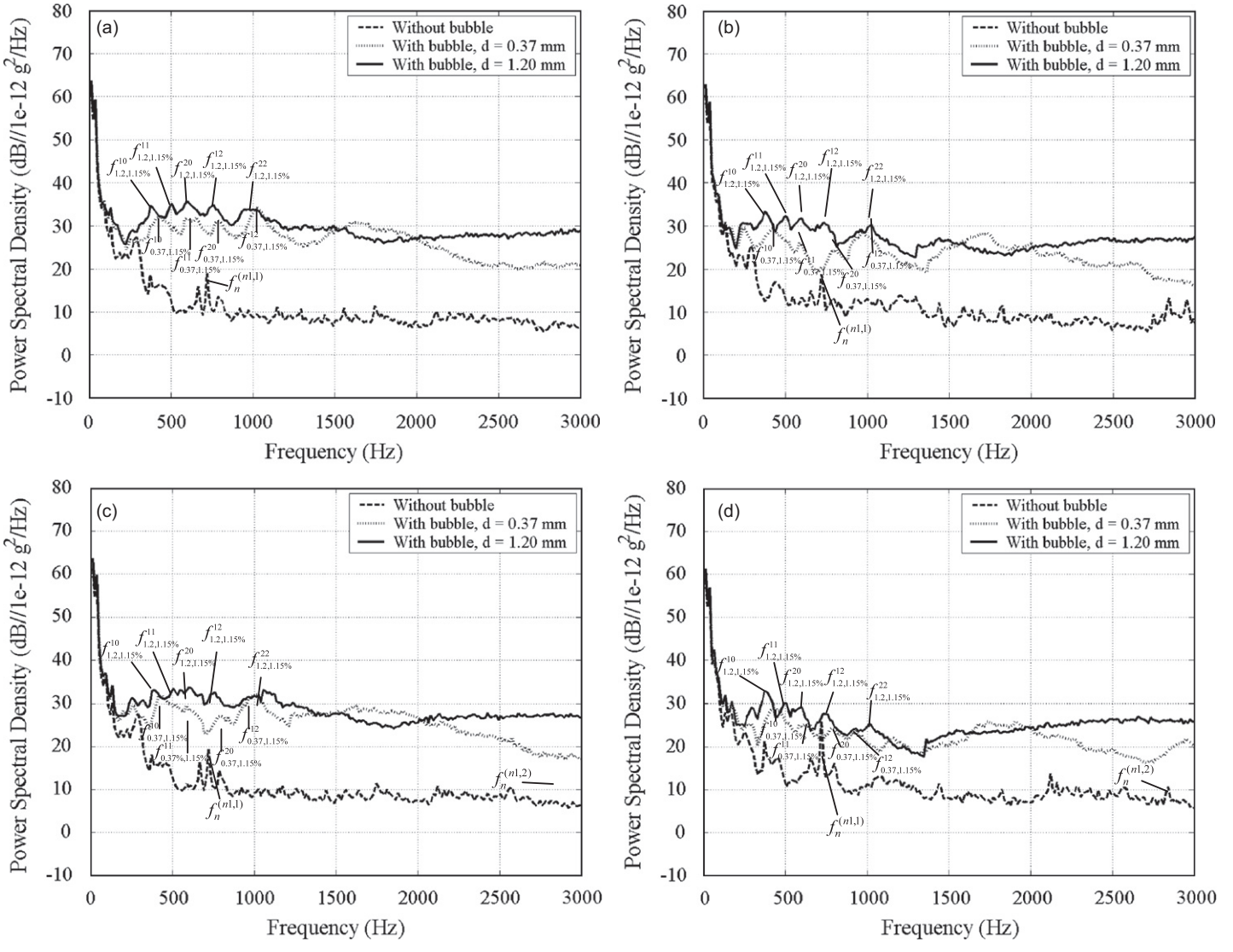

Fig. 11. Power spectral densities of plate acceleration for the same void fraction, $v = 1.15\%$, but different characteristic bubble diameters, as measured by accelerometers: (a) no. 1; (b) no. 2; (c) no. 3; (d) no. 4. $n_1 = 0$ or 1.

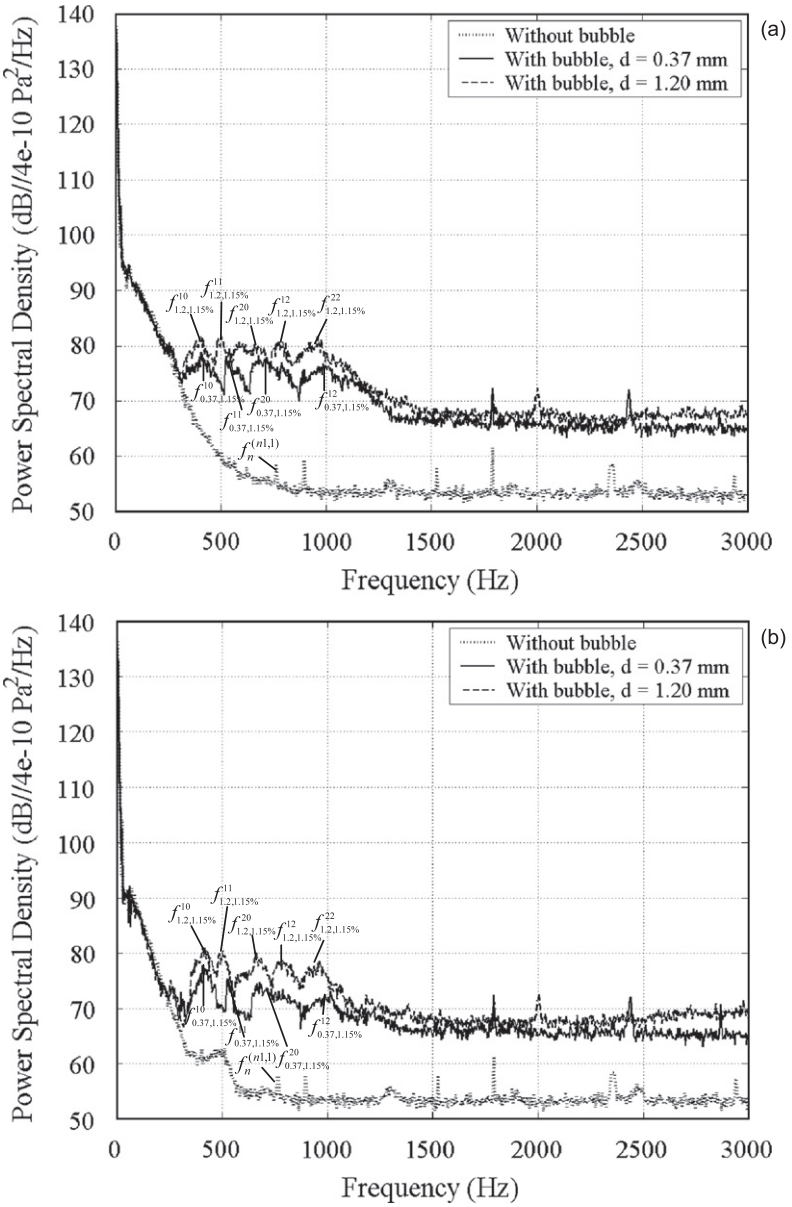

Fig. 12. Power spectral densities of wall pressure fluctuations for the same void fraction, $v = 1.15\%$, but for different bubble diameters, as measured by transducers: (a) no. 1 and (b) no. 2. $n_1 = 0$ or 1.

spectral peaks in the 300–1200 Hz range clearly decay, strongly suggesting that the origin of acoustic energy is located close to the entrance to the channel, and that this energy is attenuated while propagating through the channel. We believe that the acoustic energy is introduced by the process of bubble generation upstream of the channel. This hypothesis is strengthened by the fact that both the frequency and decay rate of these peaks can be predicted, as discussed in the following section.

The similarity between pressure and vibrations signals motivates us to examine the correlations among them. The spectral coherence $\Phi_{p'u'}$ between simultaneously measured acceleration and pressure data are calculated using (Storch and Zwiers, 1999)

$$\overline{\Phi_{p'u'}}(f) = \frac{\overline{\phi_{p'u'}(f) \cdot \phi_{p'u'}{}^*(f)}}{\overline{\phi_{p'p'}}(f) \cdot \overline{\phi_{u'u'}}(f)}, \tag{5}$$

where $\phi_{p'u'}(f)$ is the cross-spectrum between pressure and acceleration signals and the asterisk indicates its complex conjugate, while $\overline{\phi_{p'p'}}$ and $\overline{\phi_{u'u'}}$ are time averaged auto-spectra of pressure and acceleration, respectively. Fig. 13(a) displays typical results for different v but the same $d = 1.20$ mm, and Fig. 13(b) compares results for different d but the same $v = 1.15\%$, both using accelerometer 2 and pressure transducer 2 data. Clearly, before introducing bubbles, the coherence is very small at all frequencies. After introducing bubbles, the coherence at most mode frequencies, irrespective of void fraction and bubble size, increases well beyond 0.5, confirming that the same phenomena cause both the wall pressure fluctuations and vibrations. In the following section we identify their origin.

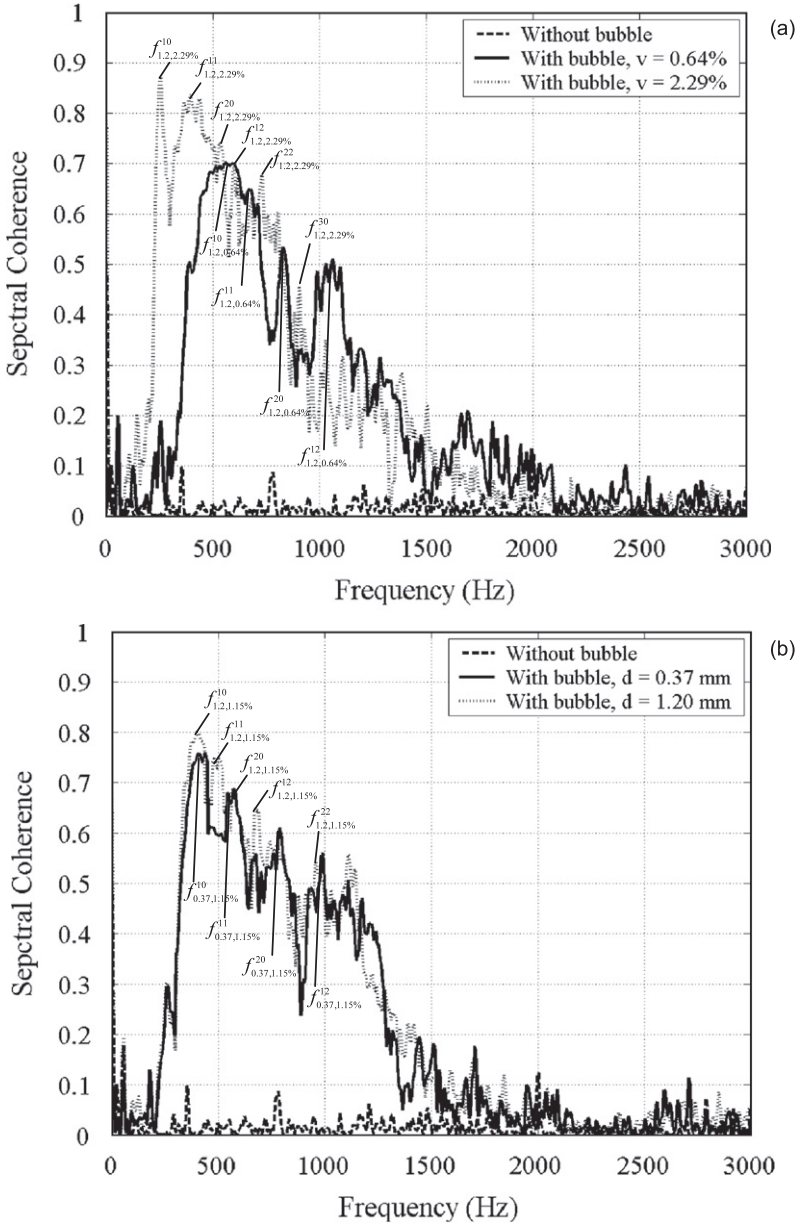

Fig. 13. Spectral coherence between plate vibrations, as measured using accelerometer 2, and wall pressure fluctuations, as measured using pressure transducer 2. Plots compare data for: (a) the same diameter (= 1.20 mm), but different void fractions, and (b) the same void fraction (= 1.15%) but different diameter.

5. Modeling the bubbly channel acoustic modes

To model the observed spectral modes and decay trends along the channel, we assume that the sound is originating from the process of bubble growth and detachment inside the settling chamber. When the supersaturated water at 1.7 MPa is injected into the settling chamber at 0.1 MPa, the bubbles grow rapidly and this process is accompanied by a strong acoustic emission. This acoustic energy is radiated into the bubbly medium with the channel walls acting as waveguides and, at the same time, excites the channel wall vibrations. To validate this hypothesis, we have constructed a model based on the infinite rigid waveguide theory (Rschevkin, 1963; Kinsler et al., 1982). This choice is justified for two reasons: First, the boundary conditions at the plates can be approximated as rigid due to the large impedance difference between plate and bubbly liquid. Second, even though the channel has a finite length, the strong attenuation of the acoustic waves makes this fact immaterial.

Fig. 1(d) shows a schematic of a long rigid channel with a square cross-section $W \times W$. Consistent with the above assumptions, a fluctuating pressure field, $p'(x,y,z,t) = p(x,y,z)e^{i\omega t}$, due to the process of bubble formation inside the settling chamber, excites the flow at the channel entrance $z = 0$. This pressure field satisfies the Helmholtz equation (Rschevkin, 1963; Commander and Prosperetti, 1989):

$$\nabla^2 p + k_m^2 p = 0, \tag{6}$$

where $k_m = \omega/c_m$ is the wavenumber in the bubbly flow that has a sonic speed of c_m. Note that we do not include a source term since the acoustic source is located outside of our modeling domain. The acoustic source is located in the settling chamber upstream of the entrance to the channel, and sound propagates into our domain through the bottom boundary. Our modeling focuses on the identification of acoustic modes associated with sound propagation through the bubbly medium in the channel. Since we assume that the walls of the channel are rigid,

$$\left(\frac{\partial p}{\partial x}\right)_{x=0} = \left(\frac{\partial p}{\partial x}\right)_{x=W} = \left(\frac{\partial p}{\partial y}\right)_{y=0} = \left(\frac{\partial p}{\partial y}\right)_{y=W} = 0, \tag{7}$$

the solution to Eq. (6), subject the above boundary conditions, is

$$p'(x,y,z,t) = \sum_{m=0}^{\infty}\sum_{n=0}^{\infty} A_{mn}\cos k_x x \cos k_y y e^{i(\omega t - k_z z)}, \quad m,n = 0,1,2,\ldots \tag{8}$$

where

$$k_x = \frac{m\pi}{W}, \quad k_y = \frac{n\pi}{W}, \quad k_z = \sqrt{k_m^2 - k_x^2 - k_y^2}, \tag{9}$$

and A_{mn} is the amplitude of the individual modes. Following Commander and Prosperetti (1989) and Lu (1990), the wavenumber k_m satisfies the dispersion relation

$$k_m^2 = \frac{\omega^2}{c_m^2} = \frac{\omega^2}{c^2} + \frac{12\nu\omega^2}{d^2(\omega_0^2 - \omega^2 + 2ib\omega)}, \tag{10}$$

where c is the sonic speed in pure water, ω_0 the angular frequency of an individual bubble ($\omega_0 = 2\pi f_0^d$, Eq. (4)) and b the effective damping constant of individual bubble oscillation; b is given by

$$b = \frac{8\mu}{\rho_w d^2} + \frac{2\overline{p}}{\rho_w d^2 \omega}\mathcal{I}m\phi + \frac{\omega^2 d}{4c}, \tag{11}$$

where μ is the viscosity of water, and ϕ is a complex function, defined in Prosperetti (1977):

$$\phi = \frac{3\gamma}{1 - 3(\gamma-1)i\chi[(i/\chi)^{0.5}\coth(i/\chi)^{0.5} - 1]}. \tag{12}$$

Here, γ is the ratio of specific heats for the gas in the bubble, $\chi = 4D_{CO_2}/\omega d^2$, and D_{CO_2} is the thermal diffusivity of CO_2. Evidently, c_m and consequently k_m and k_z are complex due to the presence of damping term b in the denominator of Eq. (10), which includes contributions of viscous, thermal and acoustic dissipation. Therefore, k_z can be expressed as

$$k_z = \alpha - \beta i, \tag{13}$$

and Eq. (8) can be rewritten as

$$p'(x,y,z,t)=\sum_{m=0}^{\infty}\sum_{n=0}^{\infty}A_{mn}\cos k_x x\cos k_y y\mathrm{e}^{-\beta z}\mathrm{e}^{i(\omega t-\alpha z)}. \tag{14}$$

The values of β, i.e., the streamwise decay rate of the sound in the channel, can be calculated using Eqs. (9)–(13). Note that Commander and Prosperetti (1989) use $c/c_m=q-ir$, and consequently, $\beta=\omega r/c$. For a certain mode, (m, n), the spatial distribution of amplitude is

$$p_{mn}(x,y,z)=\left|A_{mn}\cos k_x x\cos k_y y\right|\mathrm{e}^{-\beta z}. \tag{15}$$

Thus, for given boundary conditions, d, v, fluid and gas properties as well as location in the bubbly channel, p_{mn} is only a function of ω. Due to its dependence on β, for each mode, there is a frequency for which β is minimal, and therefore p_{mn} is maximum. This frequency can be calculated from the above equations. In practice, the sound decay rate along the channel is often expressed as an attenuation coefficient (Commander and Prosperetti, 1989),

$$A=\frac{10\log_{10}[p_{mn}(z_1)/p_{mn}(z_2)]^2}{z_2-z_1}=20\beta\log_{10}(\mathrm{e}). \tag{16}$$

Based on Eq. (16), the present attenuation coefficients are measured using the ratio of mean magnitudes of two accelerometer signals (or two transducer signals) for each frequency, as well as the distance between the two sensors. Therefore, this model enables us to calculate the normal mode frequencies, $f_{d,v}^{mn}$, of sound propagation in the channel and their corresponding attenuation coefficient. It also permits the calculation of the phase velocity, V, for each mode (Commander and Prosperetti, 1989)

$$V=1/\mathcal{R}e\left(\frac{1}{c_m}\right)=\frac{c}{q}. \tag{17}$$

Since the phase speed can be measured, as described below, results can be compared to the model predictions. Measured and calculated values of the mode frequencies, attenuation coefficients and phase speeds are compared in Tables 3 and 4, the

Table 3
Comparisons of typical measured and calculated mode frequency $f_{d,v}^{mn}$, attenuation coefficient A and phase speed V, for the same characteristic bubble diameter $d=1.20$ mm but different void fraction v.

	Void fraction										
	$v=0.64\%$				$v=2.29\%$						
Mode frequency	$f_{1.2,0.64\%}^{10}$	$f_{1.2,0.64\%}^{11}$	$f_{1.2,0.64\%}^{20}$	$f_{1.2,0.64\%}^{12}$	$f_{1.2,2.29\%}^{10}$	$f_{1.2,2.29\%}^{11}$	$f_{1.2,2.29\%}^{20}$	$f_{1.2,2.29\%}^{12}$	$f_{1.2,2.29\%}^{22}$	$f_{1.2,2.29\%}^{30}$	$f_{1.2,2.29\%}^{32}$
Calculated $f_{d,v}^{mn}$ (Hz)	518	717	959	1052	276	389	539	597	754	796	939
Measured $f_{d,v}^{mn}$ from accelerometer data (Hz)	500	665	866	1025	254	400	506	580	707	793	917
Measured $f_{d,v}^{mn}$ from transducer data (Hz)	525	690	840	1050	260	340	493	545	647	795	
Calculated A (dB/m)	4.08	7.82	10.30	11.72	2.18	4.24	5.79	6.66	8.11	8.87	10.99
Measured A from accelerometer data (dB/m)	3.67	8.16	9.32	11.18	1.83	3.86	5.26	5.81	7.34	8.64	10.16
Measured A from transducer data (dB/m)	4.01	8.03	9.47	10.59	1.82	4.12	5.17	5.92	7.31	8.46	
Calculated V (m/s)	123.9	123.2	121.9	121.4	66.0	65.9	65.7	65.5	65.2	65.1	64.7
Measured V from accelerometer data (m/s)	124	111.5	113.4	109.9	68.2	66.0	64.4	59.0	58.9	55.9	54.5
Measured V from transducer data (m/s)	125.8	122.3	112.8	118.8	61.2	63.8	64.4	58.3	56.3	59.3	

Table 4
Comparisons of typical measured and calculated mode frequency $f_{d,v}^{mn}$, attenuation coefficient A and phase speed V, for the same void fraction $v = 1.15\%$ but different characteristic bubble diameter d.

	Diameter								
	$d = 0.37$ mm				$d = 1.20$ mm				
Mode frequency	$f_{0.37,1.15\%}^{10}$	$f_{0.37,1.15\%}^{11}$	$f_{0.37,1.15\%}^{20}$	$f_{0.37,1.15\%}^{12}$	$f_{1.2,1.15\%}^{10}$	$f_{1.2,1.15\%}^{11}$	$f_{1.2,1.15\%}^{20}$	$f_{1.2,1.15\%}^{12}$	$f_{1.2,1.15\%}^{22}$
Calculated $f_{d,v}^{mn}$ (Hz)	408	549	746	834	384	522	699	770	991
Measured $f_{d,v}^{mn}$from accelerometer data (Hz)	422	600	818	935	399	524	635	718	870
Measured $f_{d,v}^{mn}$from pressure transducer data (Hz)	410	565	801	925	405	503	602	740	860
Calculated A (dB/m)	4.86	8.19	12.38	14.28	4.10	5.90	7.94	9.07	10.97
Measured A from accelerometer data (dB/m)	4.31	8.4	11.51	14.62	3.56	4.89	7.44	8.57	9.82
Measured A from pressure transducer data (dB/m)	4.12	8.68	12.43	14.95	3.61	5.19	7.11	8.10	10.37
Calculated V (m/s)	93.3	93.3	93.3	93.3	92.9	92.6	92.1	91.9	91.0
Measured V from accelerometer data (m/s)	99.2	98.0	97.7	98.8	89.6	82.8	81.2	82.1	83.5
Measured V from transducer data (m/s)	92.0	82.7	88.6	95.6	89.9	83.9	81.1	83.7	90.6

first for a fixed characteristic bubble diameter (d=1.20 mm) and varying void fraction, and the second for a fixed void fraction ($v = 1.15\%$) and varying diameter.

In the present analysis, we assume an infinitely long channel by ignoring the possibility of reflected waves. This assumption can be supported by noting that the total length of the channel is 2 m, but the tube carrying the bubbly liquid to the storage tank is at least 3 m longer. With attenuation coefficients varying between 4 and 12 dB/m, i.e., the amplitude of a reflected wave in the storage tank would be weaker than the original wave by 20–60 dB, namely a factor of 10–1000, respectively. Consequently, it is reasonable to assume that the channel is infinitely long.

6. Comparisons of modeled and measured trends

We start by comparing the measured and modeled phase velocity. The phase velocity corresponding to $f_{d,v}^{mn}$, can be estimated from the experimental data using

$$V = \frac{2\pi f_{d,v}^{mn} \Delta z}{\theta}, \tag{18}$$

where θ is the phase shift at $f_{d,v}^{mn}$ between two simultaneously measured accelerometer or transducer signals, numbers 1 and 2 in the present analysis. The values of θ can be calculated using (Storch and Zwiers, 1999)

$$\theta = \tan^{-1} \frac{\mathcal{I}m[\overline{\phi_{p'(z_2)p'(z_1)}(f)}]}{\mathcal{R}e[\overline{\phi_{p'(z_2)p'(z_1)}(f)}]} + 2N\pi. \tag{19}$$

Here $\mathcal{R}e[\overline{\phi_{p'(z_2)p'(z_1)}(f)}]$ and $\mathcal{I}m[\overline{\phi_{p'(z_2)p'(z_1)}(f)}]$ are the real and imaginary parts of the time averaged cross-spectrum of pressure signals (the same applies to vibration signals) and N is an integer, needed when the distance between sensors is larger than the wavelength. We have used the data of both pressure and vibrations transducers to measure the phase velocity, and results are compared to the model predictions in Fig. 14, as well as in Tables 3 and 4. As is evident, differences between modeled and measured speeds are for most cases less than 10%, a clear agreement considering the approximated method used for measuring the sound speed, and the (expected) substantial difference between results and the speed of sound in pure water. Trends with void fraction and bubble diameter also agree, although the measured effect of changing diameter is larger than modeled trends.

Comparisons between modeled and measured mode frequencies and attenuation coefficients are presented in Figs. 15 and 16 and tabulated in part in Tables 3 and 4. Clearly, for all the modes and both sensors, the modeled and measured $f_{d,v}^{mn}$ and A as well as their trends with diameter and void fraction are very close to each other. Due to the consistent close

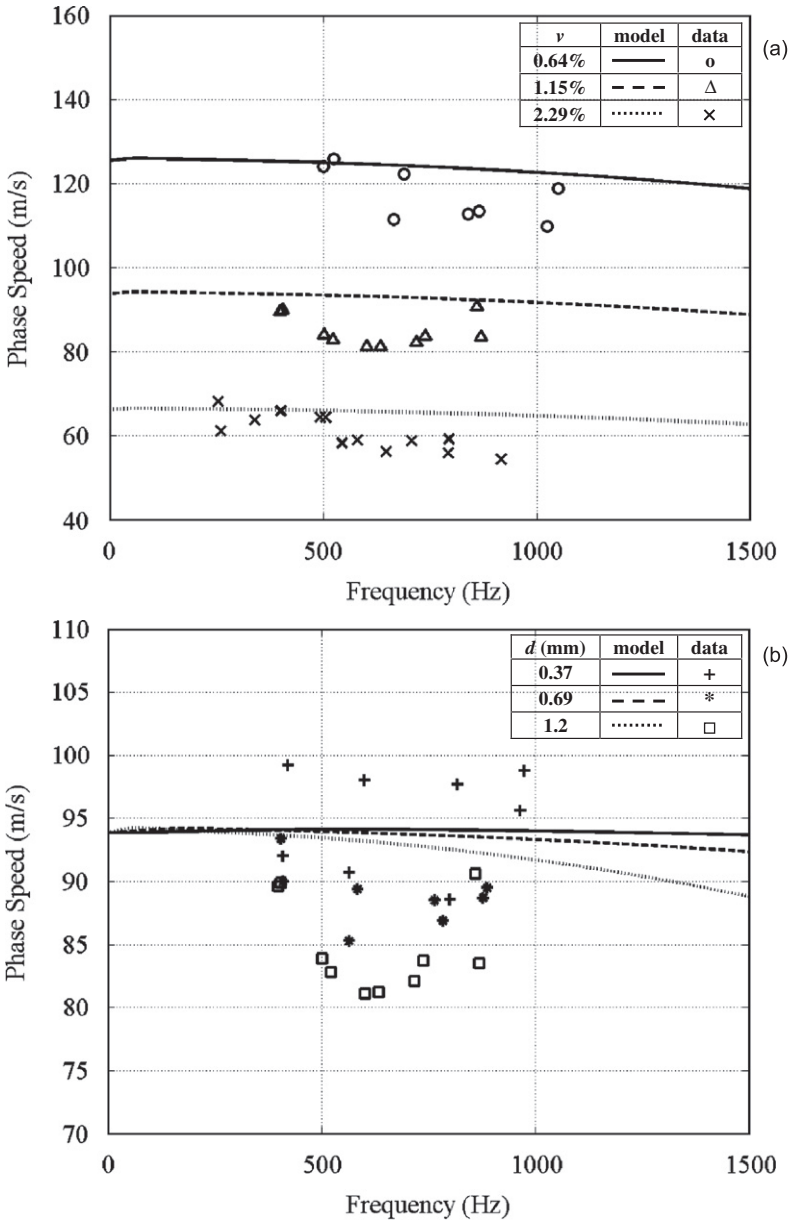

Fig. 14. Comparisons of typical measured (symbols) and calculated (lines) phase speed at different mode frequencies for (a) the same characteristic bubble diameter, $d = 1.20$ mm, but different void fractions, (b) the same void fraction, $v = 1.15\%$, but different bubble diameters. Accelerometer and pressure transducer results use the same symbol since the difference between them is very small.

agreement between the transducer and accelerometer values, there is not even a reason to use different symbols for them. Thus, we opt to present the data using the same symbols to improve the clarity of these figures. Several trends can be observed from the results as follows.

(i) Figs. 15(a) and 16(a) demonstrate that for the same bubble diameter, 1.2 mm in the shown example, both the mode frequency and attenuation coefficient decrease significantly with increasing void fraction. The same trends persist for the other diameters (not shown).

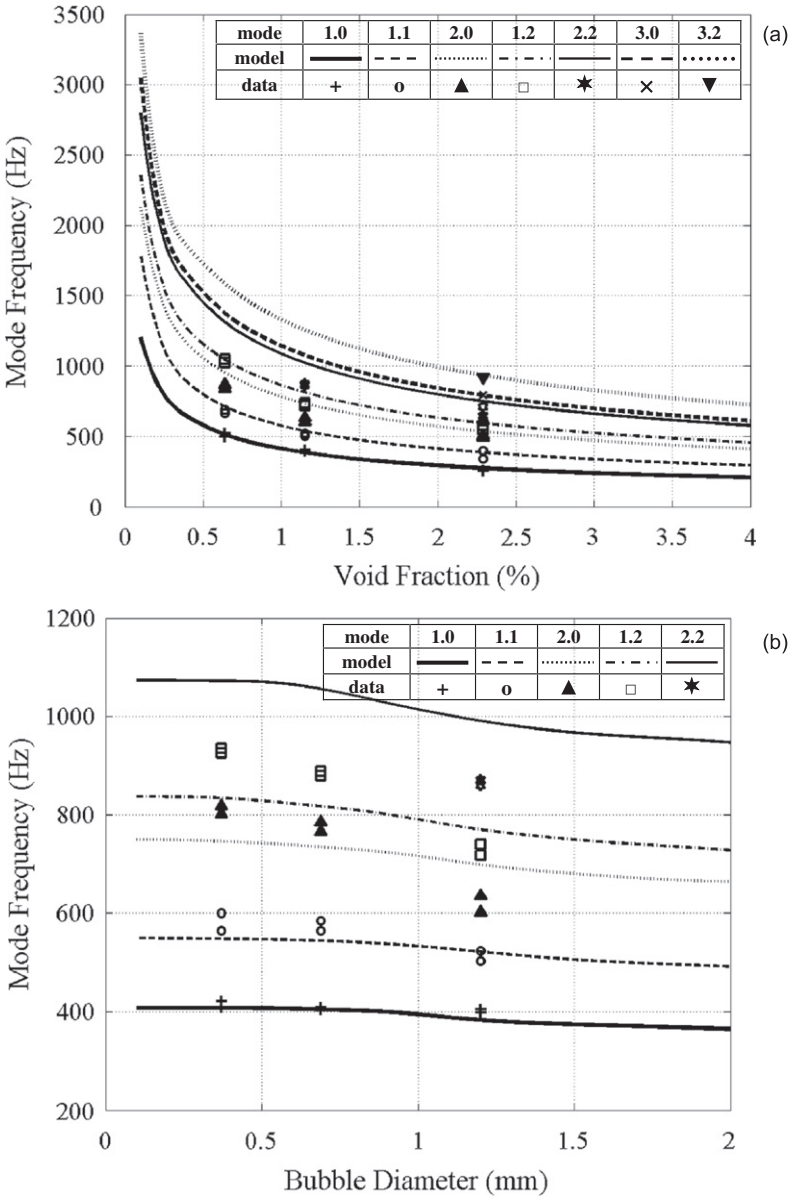

Fig. 15. Comparisons of measured (symbols) and calculated (lines) mode frequencies for (a) the same bubble diameter, $d = 1.20$ mm, but different void fractions, (b) the same void fraction, $v = 1.15\%$, but different bubble diameters. Accelerometer and pressure transducer results use the same symbol since the difference between them is very small.

(ii) Figs. 15(b) and 16(b) show that for the same void fraction, 1.15% in the shown example, both the mode frequency and attenuation coefficient decrease with increasing bubble diameter. Again, these trends persist for the other void fractions (not shown). However, the effect of bubble diameter on the mode frequency is very weak, much weaker than the impact of void fraction, as mentioned before while examining the spectra in Figs. 9–12.

(iii) For the same void fraction and/or diameter, the attenuation coefficient increases with increasing mode number. In other words, in the 250–1200 Hz range, the decay rates of the wall pressure fluctuations and vibration accelerations increase with increasing frequency. Consequences of this trend are evident by comparing spectra of accelerometers 1–4 and transducers 1–2. Similar trends of decay are predicted by a model developed by Lu (1990) for a comparable range of d and v, but for an one-dimensional bubbly layer in an infinite medium.

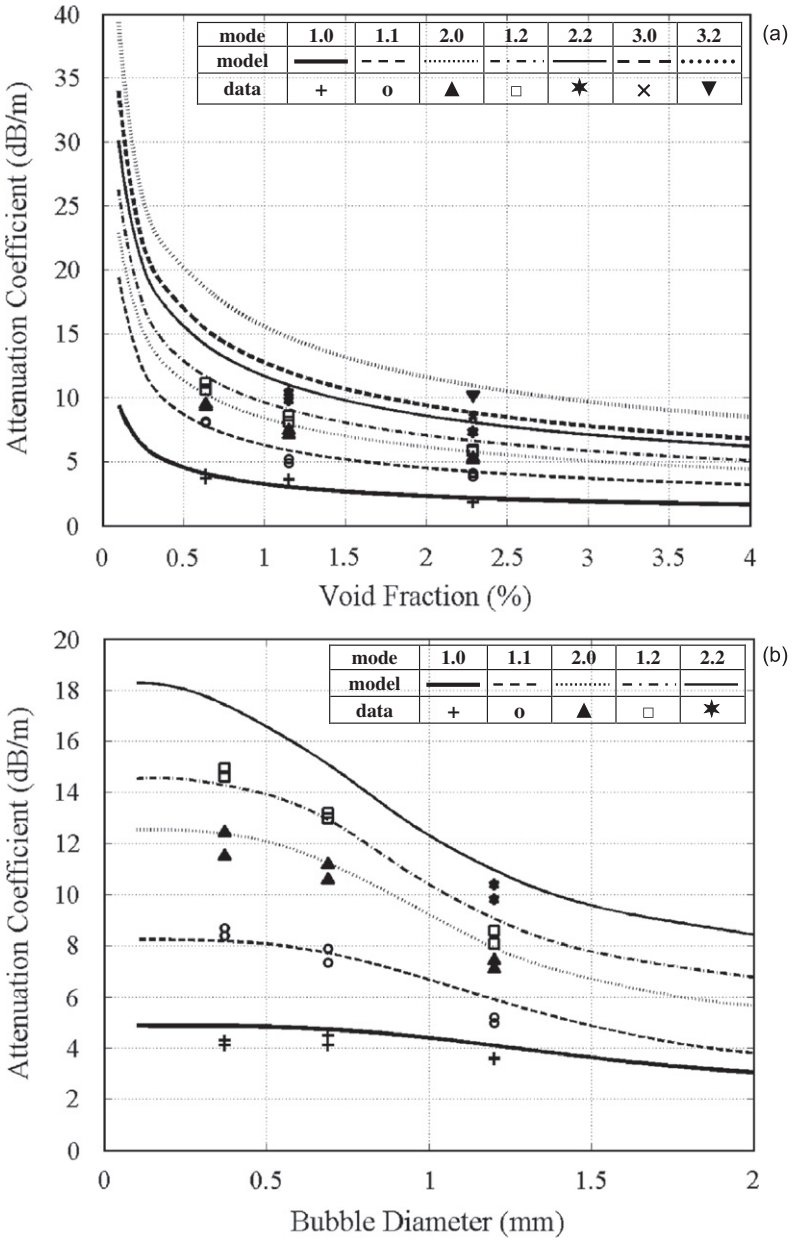

Fig. 16. Comparisons of measured (symbols) and calculated (lines) attenuation coefficients for (a) the same characteristic bubble diameter, $d = 1.20$ mm, but different void fraction, (b) the same void fraction, $v = 1.15\%$, but different bubble diameter. Accelerometer and pressure transducer results use the same symbol since the difference between them is very small.

7. Summary and conclusions

This paper examines the characteristics of channel wall vibrations induced by internal bubbly flow as well as the physical phenomena causing them. Measurements of channel wall vibrations and wall pressure fluctuations at several locations, void fractions and bubble diameters are followed by developing a mathematical model for the observed trends.

Introduction of bubbles, even at low void fractions, enhances the power spectral density of the channel wall vibrations in the 250–1200 Hz range by up to 27 dB, and the overall rms value of vibrations by up to 14.1 times,

compared with no bubble case. For the same frequency range, the wall pressure fluctuations increase by up to 26 dB, and the overall rms value by up to 12.7 times. In frequency ranges that are lower than the resonant frequency of individual bubbles, the intensity of vibrations and frequency of spectral peaks vary substantially with void fraction, and to a lesser extent with bubble size. Additional weaker spectral peaks develop at higher frequencies, in some cases (but not always) close to the plate modes and/or at the resonant frequencies of individual bubbles. Possible mechanisms are discussed briefly, including enhancement of turbulence in the bubbly flow, which, in turn enhances the vibrations, as well as excitation of plate modes by acoustic energy produced by bubbles. Further studies will focus on this range.

For the spectral peaks detected in the 300–1200 Hz range, the origin of enhanced vibrations and wall pressure fluctuations by bubbles is traced back to the generation of bubbles in the facility, which provides the energy source for subsequent processes. This energy propagates along the channel, excites specific channel modes, and interacts with the bubbly medium. A model based on waveguide theory, i.e., a solution to the 3-D Helmholtz equation in an infinitely long channel, and the physical properties of bubbles, is used to predict the frequency of spectral peaks and their attenuation coefficients. These peaks correspond to the frequency of least attenuated channel modes.

The trend of the mode frequencies, and corresponding attenuation coefficients and phase velocities with void fraction, bubble diameter and frequency are well predicted by the model. For the same mode, the smaller the void fraction and bubble diameter, the higher the mode frequency, phase velocity and decay rate. However, the effect of bubble diameter on these trends is much weaker than that of the void fraction. For the same void fraction and bubble diameter, the higher the mode frequency, the faster the mode decays.

Acknowledgements

This project was funded by the Office of Naval Research under Grant no. N00014-06-1-0333. The program officers have been Stephen Schreppler, William Martin, and presently, Deborah Nalchajian. We would like to thank William Blake for discussions and suggestions, as well as our engineers, Yury Ronzhes and Steve King, and previous students, Angela Pelletier and Ian McKelvey, for constructing the facility and for their support during the experiments.

References

Carroll, J.J., Slupsky, J.D., Mather, A.E., 1991. The solubility of carbon dioxide in water at low pressure. Journal of Physical and Chemical Reference Data 20, 1201–1209.

Commander, K.W., Prosperetti, A., 1989. Linear pressure waves in bubbly liquids: comparison between theory and experiments. Journal of the Acoustical Society of America 85, 732–746.

Emery, W.J., Thomson, R.E., 1997. In: Data Analysis Methods in Physical Oceanography. Pergamon, New York.

Feenstra, P.A., Judd, R.L., Weaver, D.S., 1995. Fluidelastic instability of a tube array subjected to two-phase R-11 cross-flow. Journal of Fluids and Structures 9, 747–771.

Genta, G., 1999. In: Vibration of Structures and Machines: Practical Aspects third ed. Springer-Verlag, New York pp. 124–128.

Gopalan, S., Abraham, B.M., Katz, J., 2002. Flow structure, pressure fluctuations and resulting vibrations caused by the interaction of a turbulent jet with cross flow over a flexible flat plate. In: Proceedings of the Fifth International Symposium on Fluid–structure Interactions, Aeroelasticity, Flow-induced Vibration and Noise, International Mechanical Engineering Congress and Exhibition, IMECE2002-32225.

Gopalan, S., Abraham, B., Katz, J., 2004. The structure of a jet in cross flow at low velocity ratios. Physics of Fluids 16, 2067–2087.

Gorman, D.J., 1971. An analytical and experimental investigation of the vibration of cylinder reactor fuel elements in two-phase parallel-flow. Nuclear Science and Engineering 44, 277–290.

Heilker, W.J., Vincent, R.Q., 1981. Vibration in nuclear heat exchanger due to liquid and two-phase flow. ASME Journal of Engineering for Power 103, 358–365.

Iijima, T., Hara, F., Nishikubo, K., 1995. Unsteady fluid force acting on 2 tandem circular-cylinders subjected to 2-phase cross-flow. JSME International Journal Series C-Dynamics Control Robotics Design and Manufacturing 38, 219–226.

Joo, J., Dhir, V.K., 1994. An experimental study of drag on a single tube and on a tube in an array under two-phase cross flow. International Journal of Multiphase Flow 20, 1009–1019.

Kinsler, L.E., Frey, A.R., Coppens, A.B., Sanders, J.V., 1982. In: Fundamentals of Acoustics. Wiley Inc., New York.

Lance, M., Bataille, J., 1991. Turbulence in the liquid-phase of a uniform bubbly air water-flow. Journal of Fluid Mechanics 222, 95–118.

Lu, N.Q., 1990. Bubble clouds as sources and scatters of underwater sound. Ph.D. Thesis, The Johns Hopkins University, Baltimore, MD, USA.

Mann, W., Mayinger, F., 1995. Flow-induced vibration of tube bundles subjected to single- and two-phase cross-flow. In: Proceedings of the Second International Conference on Multiphase Flow, Kyoto, Japan, pp. 9–15.

Martínez-Bazán, C., Montañés, J.L., Lasheras, J.C., 1999. On the breakup of an air bubble injected into a fully developed turbulent flow. Part 1. Breakup frequency. Journal of Fluid Mechanics 401, 157–182.

Merkle, C.L., Deutsch, S., 1992. Microbubble drag reduction in liquid turbulent boundary layers. Applied Mechanics Reviews 45, 103–127.

Nakamura, T., Hirota, K., Watanabe, Y., Mureithi, N.W., Kusakabe, T., Takamatsu, H., 2002. Dynamics of an in-line tube array subjected to steam-water cross-flow, Part I: two-phase damping and added mass. Journal of Fluids and Structures 16, 123–136.

Oğuz, H.N., 1994. A theoretical study low-frequency oceanic ambient noise. Journal of the Acoustical Society of America 95, 1895–1912.

Pelletier, A.R., Mckelvey, I.A., Katz, J., 2006. Effect of bubbles on flow induced vibration. In: ASME Pressure Vessels and Piping Division Conference, Vancouver, BC, Canada, July 23–27, PVP2006-ICPT11-93968.

Pettigrew, M.J., Gorman, D.J., 1981. Vibration of heat exchanger tube bundles in liquid and two-phase cross flow. In: Chen, P.Y. (Ed.), Flow-induced Vibration Design Guidelines, ASME, PVP, vol. 52, pp. 89–110.

Pettigrew, M.J., Tromp, J.H., Mastorakos, J., 1985. Vibration of tube bundles subjected to two-phase cross-flow. ASME Journal of Pressure Vessel Technology 107, 335–343.

Pettigrew, M.J., Taylor, C.E., 1994. Two-phase flow-induced vibration: an overview. ASME Journal of Pressure Vessel Technology 116, 233–253.

Pettigrew, M.J., Taylor, C.E., Kim, B.S., 2001. The effects of tube bundle geometry on vibration in two-phase cross flow. Special FSI Issue of ASME Journal of Pressure Vessel Technology 123, 414–420.

Pettigrew, M.J., Taylor, C.E., Janzen, V.P., Whan, T., 2002. Vibration behavior of rotated triangular tube bundles in two-phase cross flows. ASME Journal of Pressure Vessel Technology 124, 144–153.

Pettigrew, M.J., Zhang, C., Mureithi, N.W., Pamfil, D., 2005. Detailed flow and force measurements in a rotated triangular tube bundle subjected to two-phase cross-flow. Journal of Fluids and Structures 20, 567–575.

Plesset, M.S., Prosperetti, A., 1977. Bubble Dynamics and Cavitation. Annual Review of Fluid Mechanics 9, 145–185.

Prosperetti, A., 1977. Thermal effects and damping mechanisms in the forced radial oscillations of gas bubbles in liquids. Journal of the Acoustical Society of America 61, 17–27.

Rschevkin, S.N., 1963. In: The Theory of Sound. The Macmillan Company, New York.

Schiller, L., Naumann, A., 1933. Fundamental calculations in gravitational processing. ZEITSCHRIFT DES VEREINES DEUTSCHER INGENIEURE 77, 318–320.

Shawkat, M.E., Ching, C.Y., Shoukri, M., 2007. On the liquid turbulence energy spectra in two-phase bubbly flow in a large diameter vertical pipe. International Journal of Multiphase Flow 33, 300–316.

Shen, X.C., Ceccio, S.L., Perlin, M., 2006. Influence of bubble size on micro-bubble drag reduction. Experiments in Fluids 41, 415–424.

Sridhar, G., Katz, J., 1995. Drag and lift forces on microscopic bubbles entrained by a vortex. Physics of Fluids 7, 389–399.

Storch, H.V., Zwiers, F.W., 1999. In: Statistical Analysis in Climate Research. Cambridge University Press, Cambridge, UK pp. 234–241.

Tkalich, P., Chan, E.S., 2002. Breaking wind waves as a source of ambient noise. Journal of the Acoustical Society of America 112, 456–463.

Uchiyama, T., 2003. Numerical prediction of added mass and damping for a cylinder oscillating in confined incompressible gas–liquid two-phase mixture. Nuclear Engineering and Design 222, 68–78.

Weaver, D.S., Fitzpatrick, J.A., 1988. A review of cross-flow induced vibrations in heat exchanger tube arrays. Journal of Fluids and Structures 2, 73–93.

Weaver, D.S., Ziada, S., Au-Yang, M.K., Chen, S.S., Païdoussis, M.P., Pettigrew, M.J., 2000. Flow-induced vibrations in power and process plant components-progress and prospects. ASME Journal of Pressure Vessel Technology 122, 339–348.

Zhang, M.M., Katz, J., 2007. Vibration behavior of a channel subjected to an internal two-phase flow. In: ASME Pressure Vessels and Piping Division Conference, San Antonio, TX, USA, July 22–26, PVP2007-26655.